2017 IEEE International Conference on Robotics and Automation (ICRA)
Singapore, May 29 - June 3, 2017

Design and Experiments for a Transformable Solar-UAV

Ruben D'Sa, Travis Henderson, Devon Jenson, Michael Calvert, Thaine Heller,
Bobby Schulz, Jack Kilian, and Nikolaos Papanikolopoulos
{ dsaxx005 | hende471 | jens1172 | calve046 | helle219 | schu3119 | kilia025 }@umn.edu, {npapas}@cs.umn.edu
Department of Computer Science and Engineering, University of Minnesota

***Abstract*— Aerial robotic platforms are an increasingly sought-after solution for a variety of sensing, monitoring, and transportation challenges. However, as invaluable as unmanned aerial vehicles (UAVs) have been for these applications, fixed-wing and multi-rotor systems each have individual limitations. Fixed-wing UAVs are generally capable of high-altitude surveillance and long flight times, while quad-rotors are most effective when used for their maneuverability and close-quarters surveying.**

This paper improves upon the prototypes discussed in [1] by creating a series of three next-generation prototypes to isolate the aspects of solar powered fixed-wing flight, quad-rotor flight, and transformation modes of the SUAV:Q platform. Improvements to the transformation mechanism, airframe design, variable pitch propulsion system, and custom-designed power electronics are presented along with validation of the designs through empirical testing.

I. Introduction

Across a wide range of industries, the use of UAV technology has been instrumental in furthering research and commercial applications. Its usefulness has been proven in domains ranging from remote sensing in [2] and [3], to precision agriculture in [4] and [5], and environmental monitoring in [6]. UAVs also have applications in search and rescue, as described in [7] and [8], and air quality monitoring in [9] and [10]. As the demand for this technology increases, the range of problems needing a solution broadens. To meet this growing demand, systems must become more flexible and robust, and new solutions have to be developed to work around the limitations of traditional UAVs.

Across many of these domains, a common choice that must be made is in the selection of an aerial platform. In [11], authors discuss the advantages and disadvantages of using rotor-wing and fixed-wing UAVs in remote sensing applications. While their rotor-wing had vertical take-off and landing (VTOL) capability, it suffered from endurance and speed limitations. In contrast, their fixed-wing platform exhibited a significantly higher payload capacity and maximum endurance, but required a runway for take off and landing. The vision of the Solar UAV Quad (SUAV:Q) platform is to support researchers by providing a system capable of combining the best of both rotor-wing and fixed-wing platforms, offering the maneuverability and VTOL capability of a quad-rotor with the efficiency of a fixed-wing UAV.

The advances in high efficiency, commercially available solar cells combined with the wide availability of brushless DC motors, composite materials, and high-performance flight controllers, have made it possible to design small-scale

(a)

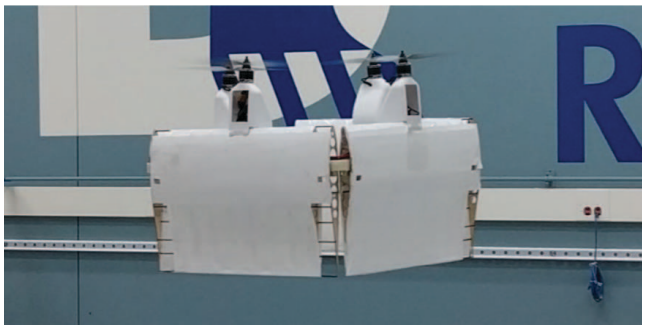

(b)

Fig. 1: (a) SUAV:Q airframe flying in fixed-wing configuration. **(b)** SUAV:Q airframe flying in quad-rotor configuration.

UAVs capable of day-long and multi-day fight. The recent pursuit of small-scale solar powered UAVs is discussed in [12], [13], and [14]. The SUAV:Q platform leverages the energy collection in a fixed-wing solar powered state to augment the energy expense of its quad-rotor state. By performing ground-to-ground, ground-to-air, and air-to-air transformations from quad-rotor to fixed-wing states, the system can transition from operating in a state that draws significantly more power than what solar can provide (quad-rotor) into a state where solar power availability is significantly higher than cruise power consumption (fixed-wing). This augmentation of energy collection and expenditure allows for the SUAV:Q platform to provide extended flight time and endurance across all states. A discussion of SUAV:Q concept and energy framework is first discussed in [15] with the work in [1] focusing on major design improvements in the area of the airframe, propulsion system, and power electronics.

VTOL capability increases the versatility of UAVs, but is traditionally approached in ways described in [16] along with perching methods such as in [17], and tail-sitting approaches

discussed in [18]. The proposed approach in the SUAV:Q design uses three servo-driven 4-bar hinge mechanisms connected between the four wing sections. In addition to the hinges, the propulsion system and control surfaces are used to transform the UAV between quad-rotor and fixed-wing states. The intent with pursuing this approach over others is to provide the greatest control authority in the quad-rotor state while also supporting a high-aspect ratio fixed-wing design. This control authority can be leveraged for carrying various sensors and payloads with non-ideal weight distributions.

II. Aerial Robot Design

Utilizing the design approach discussed in [1], three prototypes were fabricated: fixed-wing solar (Figure 1a), quad-rotor (Figure 1b), and fully transformable discussed in Section II-C.

All three prototypes use the MH49 airfoil and have a chord length of 0.310 m. The three major differences in airframe design between the prototypes are the hinge design, number of control surfaces, and number of motors used for propulsion. The fixed-wing and quad-rotor prototypes used couplers that were fixed into position in place of the hinges, while the fully transformable system had fully actuated servo driven hinges. The quad-rotor prototype did not have any driven control surfaces, while the fixed-wing solar platform had two, and the fully transforming wing had four driven control surface segments. The fixed-wing solar UAV utilized only two motors, one on each of the two center sections, to simplify early fixed-wing flight tests and airframe validation. The quad-rotor and fully transformable platforms had a propulsion system on each of the four sections.

System Specifications	Value	
Fixed-wing Prototype		
Wingspan	2.15	m
Length	0.51	m
Chord Length	0.31	m
Height	0.09	m
Battery Mass	232	g
Total Mass	3863	g
Cruise Speed	12.23	m/s
Stall Speed	11.9	m/s
Quad-rotor Prototype		
Height	0.51	m
Width	0.62	m
Depth	0.62	m
Battery Mass	232	g
Total Mass	2817	g
Transformation Prototype		
Battery Mass	232	g
Total Mass	3704	g

TABLE I: Comparison of prototype specifications. Each was constructed with identical wing segments, with the hinges and varying control surface setups comprising the main differences between the prototypes.

A. Wing Geometry

The MH49 airfoil was selected for its performance with the SUAV:Q wing geometry and payload range as discussed in [1]. Center of gravity (CG) location was adjusted based on results from Xflr5 simulations [19]. As discussed in Section V-A, preliminary flight tests showed that the drag created by the enclosure modules caused a downward pitching moment that counteracted the upward aerodynamic pitching moment created by the airfoil. Due to these opposing effects, the center of gravity was placed closer to the neutral point to reduce required control surface trim and lower cruise velocity. The center of gravity and neutral point of the aircraft are shown in Figure 2. These values give the aircraft a margin of stability of 4.67%.

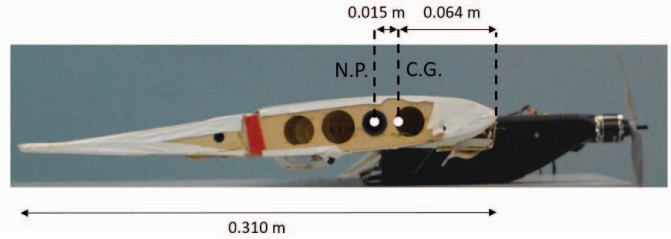

Fig. 2: Side view of the center of gravity and neutral point along airfoil.

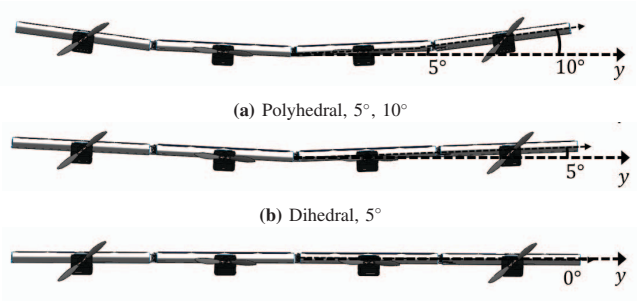

(a) Polyhedral, 5°, 10°

(b) Dihedral, 5°

(c) Plank, 0°

Fig. 3: Three fixed-wing configurations of the SUAV:Q with variation in the wing section angles.

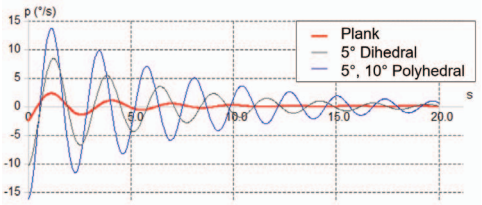

(a) Dutch roll modal analysis, roll component

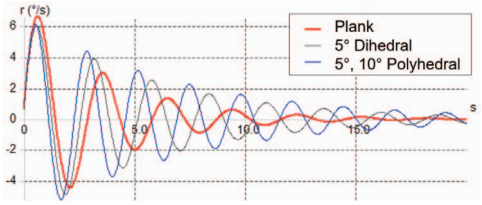

(b) Dutch roll modal analysis, yaw component

Fig. 4: Comparison of Dutch roll response in roll **(a)** and yaw **(b)** components between three potential fixed-wing configurations with varying wing section angles simulated in Xflr5. Although yaw angular rates were similar across airframes, roll rates were significantly lower for a plank wing than alternative configurations, reaching a peak roll rate of 2.5°/s in comparison to 14°/s in the case of the polyhedral.

Wing sections with varying wing section angles forming plank, dihedral, and polyhedral configurations are displayed in Figure 3. To test for optimal flight stability, the flight modes of each of the configurations were examined using Xflr5 stability analysis [19]. The results of this analysis are given in Figure 4 and show increased stability in the Dutch roll modal response as the airframe wing section angles are reduced. Given the significant reduction in oscillatory

Fig. 5: Ground transformation from quad-rotor to fixed-wing states using the transformable airframe.

yaw rate, a 0° plank wing was chosen for the fixed-wing configuration of the SUAV:Q.

B. Differential Thrust

Although the plank airframe demonstrated excellent roll stability, the lack of vertical fins resulted in challenging yaw drift and sideslip as discussed in Section V. In order to counteract these drawbacks, a proportional-integral differential thrust controller was implemented into the Pixhawk flight controller running a modified version of PX4 stack. Using the flight controller's state estimation, the aircraft yaw rate was damped by actively varying the throttle on each of the two motors used in fixed-wing flight as shown in Figure 6. By increasing the thrust from one of the motors while keeping the thrust from the alternate motor constant, a moment about the aircraft z-axis is induced. Additionally, roll and pitch inputs were mixed into the controller to perform coordinated turns. During flight trials with solar panels, differential thrust was supplemented with the addition of flat vertical fins to reduce sideslip due to heavy crosswinds. A demonstration of the differential thrust controller in use during a test flight is presented in Section V-A.

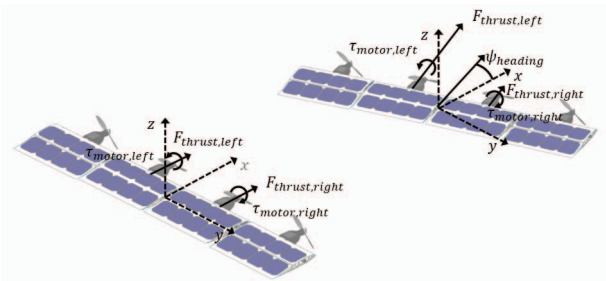

Fig. 6: Differential thrust behavior during side slip conditions. As the estimated heading deviates from the heading setpoint by angle ψ, throttle is increased to counter rotation about the z-axis.

C. Hinge Design and Transformation

To ensure stability and strength in both states, as well as a smooth in-flight transition, a robust design was needed for the hinge in between wing sections. The hinge was designed to be a double dead point 4-bar linkage. By creating dead points at the position of each of the flight configurations, the torque required by the servos to hold the aircraft rigid was significantly decreased as the coupler force vector aligned with the output to the ground axis of rotation. This mechanism was designed using graphical synthesis and implemented in Figure 5 and a model of the linkage is shown in Figure 7. Given the design choice for a 0° plank wing, a sweep of 180 degrees by the servo arm was mapped to 90 degrees by the transforming hinge linkage, distributing the servo's entire range of motion over the transformation process. This allowed for maximum utilization of servo work, as the entire input range was mapped to the output.

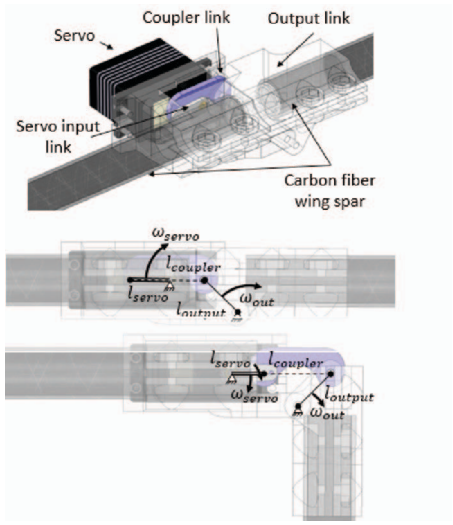

Fig. 7: CAD model of transforming hinge in fixed-wing and quad-rotor positions. As illustrated, the entire 180° servo link range is distributed across 90° of output link actuation. Pivot points were selected such that output link deadpoints occur at fixed-wing and quad-rotor states.

One of the major design constraints for the hinge is in physical size, as the design needs to be contained entirely within the narrow profile of the wing to avoid disturbing the airflow over the wing surface. The two sides of the hinge were designed to fit onto the carbon-fiber spar and then clamped using four bolts to prevent the wing sections from sliding apart. The hinge parts were fabricated using a FDM 3D printer with nylon filament and continuous fiber reinforcement. These fiber-reinforced parts were necessary for maintaining rigidity in each state and withstanding the large aerodynamic loads encountered during the transformation process. The coupler links were machined out of aluminum and shaped to avoid interfering with the servo arm in fixed-wing mode. The fully fabricated hinge is shown in Figure 8.

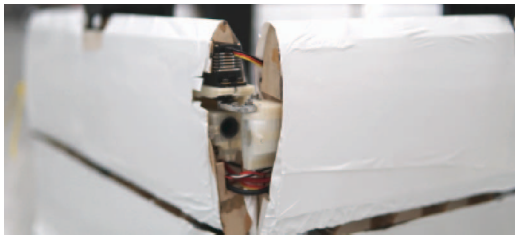

Fig. 8: Fabricated hinge installed into the transforming airframe and driven into the quad-rotor position.

III. Electronic Hardware

A block diagram outlining the connections between the solar power system, flight controller, transformation components, and actuator outputs is illustrated in Figure 9. The solar power system consists of four maximum power point trackers (MPPTs) to maximize the energy available from the solar array and support various loads in the system. Due to the unique power system requirements and high variation in solar conditions typically experienced by the SUAV:Q in fixed-wing and quad-rotor flight, custom MPPTs were designed and fabricated as discussed in [1]. To manage transition between states, two separate flight controllers were used for fixed-wing and quad-rotor flight respectively. The Pixhawk flight controller was used running a modified version of the PX4 open source firmware. To manage switching actuators between flight controllers, a 4-channel multiplexer was used with its select pin connected to the fixed-wing flight controller. Only the four propulsion motors are switched between the flight controllers. Control surface servos and transformation hinges remain connected to the fixed-wing flight controller. While in the fixed-wing state, the outer two motors are shut down to improve system efficiency.

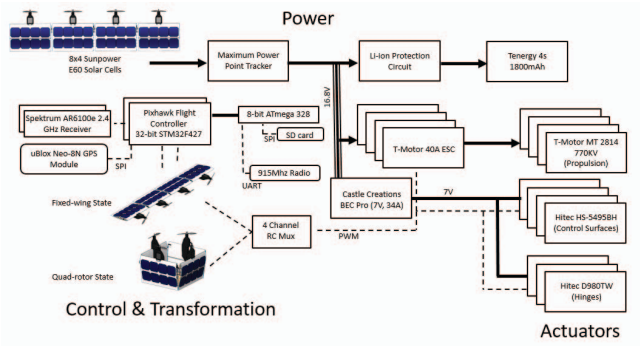

Fig. 9: Electrical topology of the aircraft

IV. Variable Pitch Propulsion

The use of a variable pitch propeller was investigated in [1] as a means of providing efficient propulsion across the SUAV:Q's wide flight envelope. Simulations showed a significant reduction in power consumption for both fixed-wing and quad-rotor states, and preliminary experiments on a proof-of-concept testbed confirmed a strong dependence of propulsion efficiency on propeller pitch. To more thoroughly validate these previous results, a propulsion system prototype was constructed to test the performance on candidate components for implementation onto the finished SUAV:Q design. Simulations were also conducted to investigate the thrust constraints of the VPP system.

A. Propulsion Prototype and Wind Tunnel Testing

Given an estimated full system mass of 4.93 kg and estimated level flight speed of 15 m/s, an APC 12x4.5MR propeller and a 770 Kv MT2814 motor were chosen. Simulations indicated that the aircraft would achieve hover at a motor speed of approximately 7000 rpm. Combining this information with the propeller's mass and moment of inertia characteristics, the radial force required to hold the propeller to the motor shaft during hover was calculated to exceed 360 N, equivalent to the weight of 37 kg. A commercially available off-the-shelf solution was not found capable of satisfying the strength, pitch range, and mechanical simplicity required for the propulsion system. An existing pitch actuation linkage was modified and fabricated to increase the strength of critical components and to modify the pitch range. To achieve these goals, a reinforced pitch clevis was designed to bear the radial force and the moments produced by propeller blade lift and drag.

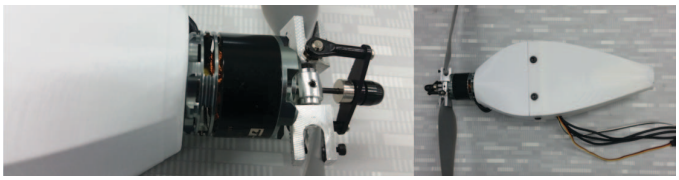

Fig. 10: Closeup of variable pitch linkage with a custom aluminum clevis and side view of a propulsion system unit and wind tunnel testing mount.

Given the combination of high radial force and aerodynamically induced bending moments, the final clevis, pictured in Figure 10 was designed to be machined out of aluminum. With this modification, the prototyped system was able to reliably exceed 9000 rpm.

To validate simulations, the 3D-printed housing pictured in Figure 10 was made to mount the propulsion prototype in a closed air return wind tunnel at the University of Minnesota, Twin Cities. The wind tunnel data acquisition system provided steady-state measurements of thrust, torque, and airspeed. Electrical voltage and current were gathered using the propulsion testbed methods discussed in [1]. Propeller blade pitch was measured by reading both the commanded position of the actuation servo and the voltage of a potentiometer which was fixed to the servo motor output shaft. Correlations between these measurements and propeller pitch were established via the mathematical relations governing four-bar linkages. To avoid creating excess drag in the wind tunnel or an imbalanced mass distribution on the propeller due to the application of reflective tape for infrared tachometry, an omnidirectional microphone was mounted in the 3D-printed wind tunnel mount to sample the frequency of mechanical vibrations created by the motor. By discerning this fundamental frequency in post-processing with a Discrete Fourier Transform, the motor's speed was calculated.

Four hundred data points were gathered from airspeeds of 0 to 20 m/s, a full range of throttle percentages, and propeller blade pitch angles from -5 to 60 degrees. The set of empirical data was compared with simulation predictions by assigning the recorded airspeed, pitch angle, and motor current as inputs to the simulator; these inputs were chosen because of the accessibility that those parameters would have on the actual airframe. In Figure 11, the mesh surface denotes the expected system efficiency ceiling as predicted by simulations. There is a significant grouping of the data to

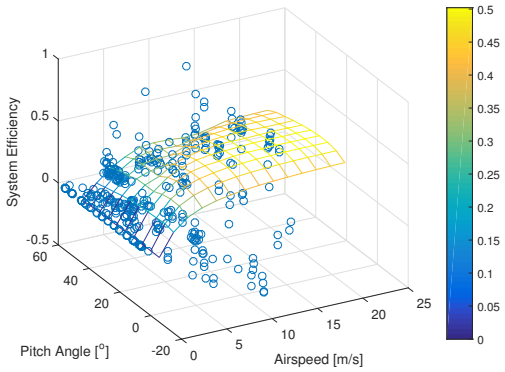

Fig. 11: Wind tunnel data of the variable pitch propulsion system superimposed on a surface describing the simulated system efficiency when the propeller pitch angle is varied to minimize consumed electrical power. Possible reasons for the disparity between experimental and simulated efficiency at extreme pitch angles include the fact that no methods were applied to correct for skin friction effects from the wind tunnel wall or for aerodynamic drag on the fixture.

the underside of this surface, indicating that the simulations provide a realistic prediction of the system efficiency when operating with power-optimal pitch. Perhaps the most obvious trend present in this raw data is that for extreme pitch angles, the empirical system efficiency diverges from the simulated prediction, and this trend increases with airspeed. One reason for this is simply that small or negative pitch angles will produce drag at higher wind speeds. Another reason for this trend is that the pitot tube in the wind tunnel used to sample airspeed is located near the wall, and thus could be under-reporting airspeed because of viscous drag effects along the wind tunnel walls. In addition, the fixture used to mount the propulsion system in the wind tunnel would produce some drag of its own, roughly proportional to the square of the airspeed. Mathematical corrections for these effects are often conducted, however, these corrections require additional wind tunnel instrumentation to construct a higher resolution model of air flow patterns, and the available test facility was not equipped with such instrumentation.

B. Maximizing Thrust

While the main benefit of the SUAV:Q propulsion system is its ability to satisfy operating condition constraints at a minimum electrical energy cost, the same hardware can also be used to pursue other optimization goals, such as maximizing the thrust at a given airspeed.

Based on work from [20], the relationship for the conversion of propeller lift and drag to thrust is defined by

$$T = \rho \int_0^R c(r)W(r)^2(C_L(r)cos(tan^{-1}(\lambda(r))) - C_D(r)sin(tan^{-1}(\lambda(r))))dr \quad (1)$$

where ρ is the density of air, and $c(r)$, $W(r)$, $C_L(r)$, and $C_D(r)$ are the local chord length, air speed, lift coefficient, and drag coefficient, respectively. The quantity $\lambda(r)$ is the local advance ratio, which describes the mixing of axial and tangential air flows that the propeller sees at a given radius along the propeller blade; a higher aircraft airspeed will result in a higher value of $\lambda(r)$.

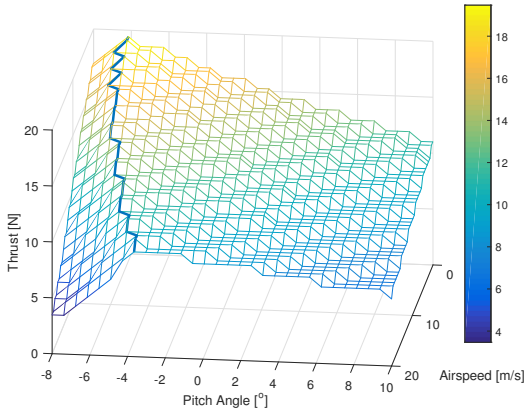

Fig. 12: Simulation of thrust optimization for a single propulsion unit of one motor-propeller pair. The airspeed was prescribed and constraints of the physical system were used to create optimization bounds on the solution space. Maximum thrust is seen at low air speeds, indicating that the direction of the total thrust vector is the dominating constraint for producing a high conversion of blade lift to thrust.

When $\lambda(r)$ is increased, the component of the total lift vector in the thrust direction decreases sinusoidally, making it harder to produce thrust in a useful direction. For this reason, high thrust values are usually seen at low airspeeds. A simulation of thrust maximization for the SUAV:Q is shown in Figure 12. It can be seen in this figure that states of max thrust are reached exclusively at pitch angles below the zero pitch angle.

V. Experimental Results

A. Fixed-Wing Flight Performance

Fixed-wing flights were performed using only two of the four propulsion pods for the purpose of airframe and controller validation. Full solar cells and solar power electronics were configured for the test flight. Figure 13 shows the relationship between the thrust differential between the two motors and the yaw rate of the aircraft as recorded by the Pixhawk autopilot running the PX4 stack with the differential thrust controller and onboard inertial measurement. High throttle input percentages of the left motor relative to the right motor indicate sideslip and heading correction due to a significant crosswind during the test flight.

Figure 14 shows a simulation of the pitching moment coefficient as a function of varying center of gravity location and velocity. Although Xflr5 simulations were used as a starting point for CG placement, several test flight iterations indicated the trimmed center of gravity was located at 0.064 m. According to the Xflr5 fixed-lift simulation, there is no possible combination of angle of attack and velocity that produces a coefficient of pitching moment of zero. The difference between the simulation and prototype results are likely attributed to sources of drag not modeled in the simulation, along with loss of airfoil curvature due to the solar cell not perfectly conforming to the airfoil surface. These sources of drag can manifest themselves as an additional downward pitching moment coefficient, shifting the pitching

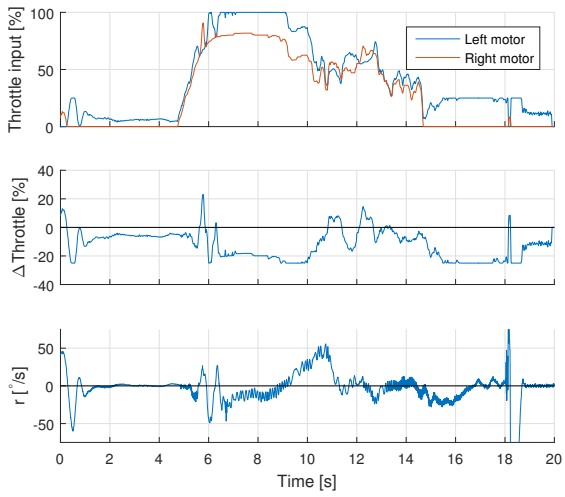

Fig. 13: Yaw rate of the fixed-wing state with the differential thrust controller enabled.

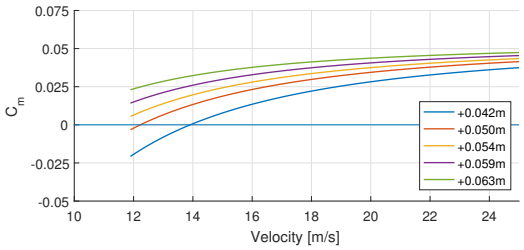

Fig. 14: Moment coefficient of the fixed-wing SUAV:Q with a system mass of 3.63kg as a function of airspeed and CG location measured from the leading edge, simulated in Xflr5.

moment coefficient curves to a region where they intersect the line $C_m = 0$, indicating a solution for level flight.

In the comparison of simulated velocity in Figure 14 and experimental cruise velocity shown in Figure 15, experimental velocity was found to be between 12m/s and 16.14m/s, higher than what was predicted from simulation, likely due to the strong cross wind which made manually trimming throttle particularly difficult and subject to over throttling.

Peak power consumption by the propulsion system during the flight reached 333.2W. While this is significantly higher than the peak solar power collected in-flight at 72.09W, the propulsion system used fixed-pitch APC 12x4.5 MR and MRP propellers designed for quad-rotor use. As discussed in Section IV, the implementation of VPP is necessary for efficient fixed-wing flight. Using the fixed-pitch propellers served their use as a reliable way to validate the airframe in fixed-wing solar configuration at the expense of propulsion system efficiency.

B. Solar Power Collection

A total of four MPPTs were used on the airframe, one for each of the four wing sections. Figure 16 shows the power from all four MPPTs in comparison with control surface position. The outer two wing sections contain control surfaces with solar cells that are exposed to differing levels of irradiance, as seen in Figures 17 and 18, depending on the control surface actuation angle. For the majority of the test flight, power from MPPT0 was significantly lower

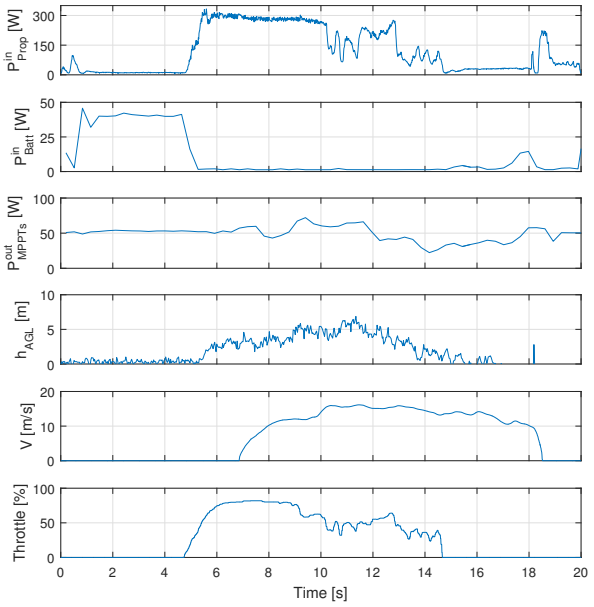

Fig. 15: Power flow during fixed-wing test flight, compared to altitude, airspeed, and throttle setting. Peak power consumption was 333.2W at take-off and the maximum cruise velocity was measured as 16.14m/s.

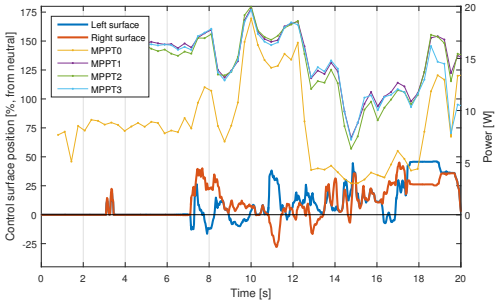

Fig. 16: Power from the SUAV:Q's solar array as measured by the MPPTs. The four MPPTs were laid out such that each tracks power input for one segment, with MPPT0 and MPPT2 on the outer control surface segments and MPPT1 and MPPT3 on the inner fixed segments. Control surface deflection is also plotted to illustrate the impact of varying solar irradiance on a single MPPT.

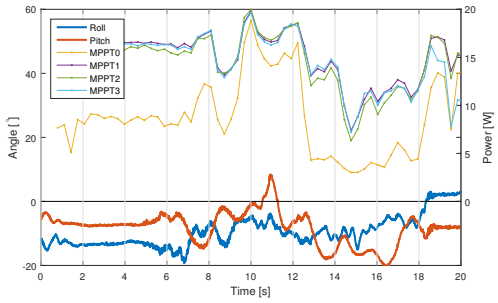

Fig. 17: Solar power collected from the SUAV:Q's solar array as compared to the roll and pitch angles of the aircraft.

than the other MPPTs. This was likely due to the shadow cast by the vertical fin on the cells MPPT0 was tracking. Upon the implementation of a more refined differential thrust controller, the vertical fins will be removed from the airframe. As shown in Figure 17, changes in aircraft roll and pitch aligns with major increases and decreases in solar power output from the MPPTs.

Fig. 18: In-flight side view of the SUAV:Q showing the control surface actuation resulting in a change in solar irradiance on the control surface.

VI. Conclusion

Presented in this paper is an overview of design and flight validation for the latest generation SUAV:Q platform. Three individual prototypes were fabricated demonstrating fixed-wing solar flight, quad-rotor flight, and ground airframe transformation. A comparison of wing configurations was performed and the modal responses of the configurations were evaluated. A 0° plank wing was chosen for the desired hinge angle due to its minimal roll rate from Dutch roll modal response. An improved transformation mechanism was designed and fabricated to facilitate ground-to-ground transformation and minimize power consumption in quad-rotor and fixed-wing configurations.

Due to limited yaw control authority, a differential thrust controller was developed to provide yaw dampening during various maneuvers in fixed-wing flight. Thrust from each of the motors was varied to create an aerodynamic moment about the aircraft's z-axis. Inertial measurement and GPS was used in state estimation to track and resolve yaw drift along with performing coordinated turns.

A VPP prototype was fabricated for wind tunnel testing; results from wind tunnel testing closely confirmed simulated predictions across pitch angles within fixed-wing and quad-rotor operating range, solidifying the justification that VPP is necessary for efficient propulsion system operation in fixed-wing and quad-rotor states. Simulation showed that the thrust ceiling of the VPP system was achieved at a narrow range of negative pitch angles.

Full solar fixed-wing flight tests were performed and used to validate power electronics operation along with airframe performance. Results from flight tests aligned with airframe simulations with regards to minimum cruise velocity and CG placement. Future iterations will pursue longer term flight tests with prototypes equipped with VPP in addition to the testing of full air-to-air transformation.

VII. Acknowledgements

This material is based upon work supported by the National Science Foundation through grants #CNS-0934327, #CNS-1439728, #IIS-1427014, #OISE-1551059, #CNS-1531330, and #CNS-1544887. Ruben DSa was supported by a National Science Foundation Graduate Research Fellowship No. 00039202.

References

[1] R. D'Sa, D. Jenson, T. Henderson, J. Kilian, B. Schulz, M. Calvert, T. Heller, and N. Papanikolopoulos, "SUAV:Q - An Improved Design for a Transformable Solar-Powered UAV," *IEEE/RSJ International Conference on Intelligent Robots and Systems (IROS)*, October 2016.

[2] J. A. Berni, P. J. Zarco-Tejada, L. Suárez, and E. Fereres, "Thermal and Narrowband Multispectral Remote Sensing for Vegetation Monitoring From an Unmanned Aerial Vehicle," *IEEE Transactions on Geoscience and Remote Sensing*, vol. 47, no. 3, pp. 722–738, 2009.

[3] U. Niethammer, M. James, S. Rothmund, J. Travelletti, and M. Joswig, "UAV-Based Remote Sensing of the Super-Sauze Landslide: Evaluation and Results," *Engineering Geology*, vol. 128, pp. 2–11, 2012.

[4] C. Zhang and J. M. Kovacs, "The Application of Small Unmanned Aerial Systems for Precision Agriculture: A Review," *Precision Agriculture*, vol. 13, no. 6, pp. 693–712, 2012.

[5] V. Gonzalez-Dugo, P. Zarco-Tejada, E. Nicolás, P. Nortes, J. Alarcón, D. Intrigliolo, and E. Fereres, "Using High Resolution UAV Thermal Imagery to Assess the Variability in the Water Status of Five Fruit Tree Species Within a Commercial Orchard," *Precision Agriculture*, vol. 14, no. 6, pp. 660–678, 2013.

[6] M. Dunbabin and L. Marques, "Robots for Environmental Monitoring: Significant Advancements and Applications," *IEEE Robotics & Automation Magazine*, vol. 19, no. 1, pp. 24–39, 2012.

[7] P. Doherty and P. Rudol, "A UAV Search and Rescue Scenario with Human Body Detection and Geolocalization," in *Australasian Joint Conference on Artificial Intelligence*. Springer, 2007, pp. 1–13.

[8] M. A. Goodrich, B. S. Morse, D. Gerhardt, J. L. Cooper, M. Quigley, J. A. Adams, and C. Humphrey, "Supporting Wilderness Search and Rescue Using a Camera-Equipped mini-UAV," *Journal of Field Robotics*, vol. 25, no. 1-2, pp. 89–110, 2008.

[9] P. Haas, C. Balistreri, P. Pontelandolfo, G. Triscone, H. Pekoz, and A. Pignatiello, "Development of an Unmanned Aerial Vehicle UAV for Air Quality Measurements in Urban Areas," in *Proceedings of the 32nd AIAA Applied Aerodynamics Conference; American Institute of Aeronautics and Astronautics, Atlanta, GA, USA*, 2014, pp. 16–20.

[10] W. Dabberdt, G. Frederick, R. Hardesty, W.-C. Lee, and K. Underwood, "Advances in Meteorological Instrumentation for Air Quality and Emergency Response," *Meteorology and Atmospheric Physics*, vol. 87, no. 1-3, pp. 57–88, 2004.

[11] J. Berni, P. Zarco-Tejada, L. Suárez, V. González-Dugo, and E. Fereres, "Remote Sensing of Vegetation from UAV Platforms Using Lightweight Multispectral and Thermal Imaging Sensors," *Int. Arch. Photogramm. Remote Sens. Spatial Inform. Sci*, vol. 38, no. 6, 2009.

[12] A. Noth, W. Engel, and R. Siegwart, "Design of an Ultra-Lightweight Autonomous Solar Airplane for Continuous Flight," in *Field and Service Robotics*, ser. Springer Tracts in Advanced Robotics, vol. 25. Springer Berlin Heidelberg, 2006, pp. 441–452.

[13] P. Oettershagen, A. Melzer, T. Mantel, K. Rudin, R. Lotz, D. Siebenmann, S. Leutenegger, K. Alexis, and R. Siegwart, "A Solar-Powered Hand-Launchable UAV for Low-Altitude Multi-Day Continuous Flight," in *IEEE International Conference on Robotics and Automation (ICRA)*, May 2015, pp. 3986–3993.

[14] S. Morton, R. D'Sa, and N. Papanikolopoulos, "Solar Powered UAV: Design and Experiments," in *IEEE/RSJ International Conference on Intelligent Robots and Systems (IROS), Hamburg*, vol. 14, no. 1, 2015, pp. 2460–2466.

[15] R. D'Sa, D. Jenson, and N. Papanikolopoulos, "SUAV:Q - A Hybrid Approach To Solar-Powered Flight," *IEEE International Conference on Robotics and Automation (ICRA)*, pp. 3288–3294, May 2016.

[16] A. S. Saeed, A. B. Younes, S. Islam, J. Dias, L. Seneviratne, and C. Guowei, "A Review on the Platform Design, Dynamic Modeling and Control of Hybrid UAVs," in *International Conference on Unmanned Aircraft Systems (ICUAS)*, June 2015, pp. 806–815.

[17] A. M. Wickenheiser and E. Garcia, "Optimization of Perching Maneuvers through Vehicle Morphing," *Journal of Guidance, Control, and Dynamics*, vol. 31, no. 4, pp. 815–823, 2008.

[18] S. Verling, B. Weibel, M. Boosfeld, K. Alexis, M. Burri, and R. Siegwart, "Full Attitude Control of a VTOL Tailsitter UAV," in *2016 IEEE International Conference on Robotics and Automation (ICRA)*, May 2016, pp. 3006–3012.

[19] A. Deperrois, "Stability Analysis Using XFLR5," http://www.xflr5.com/docs/XFLR5_and_Stability_analysis.pdf, 2010.

[20] M. Drela, "QPROP Formulation," http://web.mit.edu/drela/Public/web/qprop/qprop_theory.pdf, 2006.